Revision for Archives of Biochemistry and Biophysics
23 November 2020

Modulation of post-powerstroke dynamics in myosin II by 2'-deoxy-ADP

Matthew Carter Childers[1], Michael Geeves[2], Valerie Daggett[1], and Michael Regnier[1,*]

1. Department of Bioengineering, University of Washington, Seattle, WA 98195-5013, United States of America
2. School of Biosciences, University of Kent, Canterbury, United Kingdom

* Corresponding author

Email: mregnier@uw.edu

Running title: Post-powerstroke dynamics in myosin II

Keywords: myosin, molecular dynamics simulation, allostery

Abstract

Muscle myosins are molecular motors that hydrolyze ATP and generate force through coordinated interactions with actin filaments, known as cross-bridge cycling. During the cross-bridge cycle, functional sites in myosin 'sense' changes in interactions with actin filaments and the nucleotide binding region, resulting in allosteric transmission of information throughout the structure. We investigated whether the dynamics of the post-powerstroke state of the cross-bridge cycle are modulated in a nucleotide-dependent fashion. We compared molecular dynamics simulations of the myosin II motor domain (M) from *Dictyostelium discoideum* in the presence of ADP (M.ADP) versus 2'-deoxy-ADP bound myosin (M.dADP). We found that dADP was more flexible than ADP and the two nucleotides interacted with myosin in different ways. Replacement of ADP with dADP in the post-powerstroke state also altered the conformation of the actin binding region in myosin heads. Our results provide atomic level insights into allosteric communication networks in myosin that provide insight into the nucleotide-dependent dynamics of the cross-bridge cycle.

Introduction

Myosins are a superfamily of ATP-dependent, force-generating molecular motors that play significant biological roles in muscle contraction [1], cell adhesion and migration [2], tissue architecture [2], and cargo transport [3]. The structure of myosin is highly conserved across isoforms and across species, even though there is sequence variability [4]. Myosin heads contain four functional subdomains: the N-terminal domain, upper 50 kDa domain, lower 50 kDa domain, and the converter domain (Figure 1A-B). Each of these four subdomains interface with one another in the center of the protein in a region known as the transducer, which is a 7-stranded β-sheet [5]. Because of their ubiquity across the kingdoms of life, involvement in biological processes, and involvement in muscle diseases, there is a need to understand the molecular mechanisms that underlie force generation by these motor proteins.

Small conformational changes in the four myosin subdomains propagate through the structure and result in large conformational changes in a process known as the cross-bridge cycle [6]. The cross-bridge cycle of myosin relies on coordinated protein dynamics and can be divided into multiple steps (Figure 1C) [7]. Each of these steps is influenced by the substrates in the catalytic site, the strength of the myosin:actin interaction, the orientation of the actin-binding cleft, and the orientation of the lever arm [8,9]. The major stages of the cycle include the pre-powerstroke conformation (in which ATP has been hydrolyzed to cock the lever arm in preparation for the powerstroke), the actin-bound conformation (in which the powerstroke occurs) [10,11], the post-powerstroke conformation (after which ADP release occurs release), and the rigor conformation (which is a strongly-bound, nucleotide free state) [12]. ATP binding to the rigor conformation precipitates dissociation from actin [13]. The dynamic properties of the cross-bridge cycle can be altered by mutation or post-translational modification of the sequence

[14], by small molecules [15], or by specific nucleotides used as fuel [16,17]. A dynamic, structurally based model of the cross-bridge cycle can provide a mechanistic framework that links structural changes in contractile proteins with altered dynamic cross-bridge behavior.

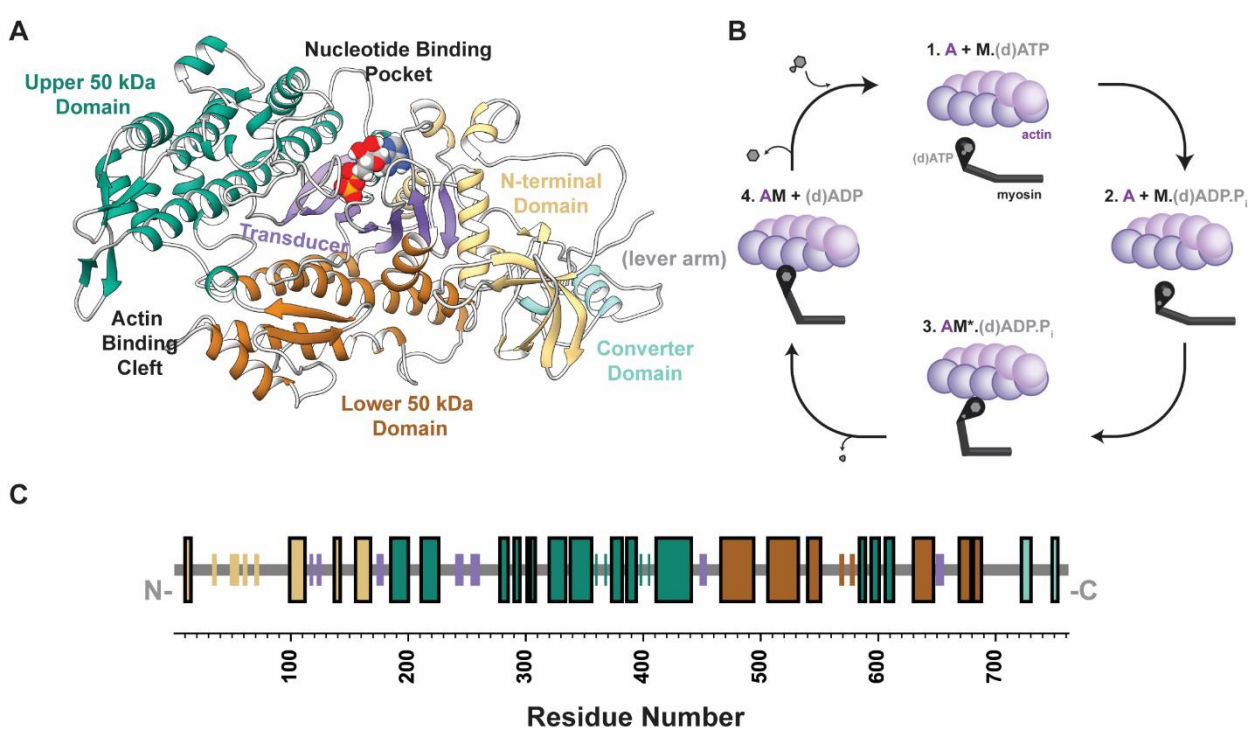

Figure 1: Structural Schematic & Sequence of Myosin. (A)The structure of the myosin head is highly conserved and can be divided into four subdomains: the N-terminal (tan), upper 50 kDa (teal), lower 50 kDa (brown), and converter (light blue) domains, and these four subdomains interface at the transducer (purple). (B) This schematic illustrates the major steps in the cross-bridge cycle. (1) The cycle begins when (d) ATP binds to myosin heads, releasing them from actin. (2) Next, (d)ATP hydrolysis primes myosin to bind actin. (3) Then, the power stroke occurs. (4) Finally, (d)ADP is released from the binding pocket. (C) The amino acid sequence is represented as a sequence of secondary structure elements (horizontal grey bars: loops, short boxes: β-strands, tall boxes: α-helices). The secondary structure elements are colored according to their respective subdomains in panel A.

X-ray crystallography of myosin has provided the structural basis for our understanding of the cross-bridge cycle. *Dictyostelium discoideum* has been the most studied model organism for studying myosin conformations [18]. At least 34 structures of *Dictyostelium discoideum* myosin II have been deposited into the Protein Data Bank (PDB, www.rcsb.org) [19] and

provide structural insights into the pre-powerstroke (e.g. PDB ID: 1VOM [20]), post-powerstroke (e.g. 1MMA [21]), rigor-like (e.g. 1FMW [22]), and post-rigor-like (e.g. 1FMV [22]) conformations. However, those structures are static snapshots of an inherently dynamic motor. Molecular dynamics (MD) simulations complement structural studies by elucidating time-dependent structural changes in myosin. Furthermore, MD simulations are a useful tool to probe how structural changes or small molecules affect the structure and dynamics of myosin.

Myosin derives the energy needed to generate force by catalyzing ATP to ADP + P_i; it is a promiscuous enzyme and can utilize numerous nucleotides as substrate. The naturally occurring nucleotide 2'-deoxy-ATP (dATP) is one such nucleotide and it increases the hydrolytic activity of skeletal [16] and cardiac [23] myosin, increases the magnitude and rate of contraction in multiple model systems, [16,17,23–27] and delays force decay during relaxation [28]. For these reasons, dATP is being investigated as a therapeutic small molecule to treat hypo-contractility associated with heart failure. During contraction, dATP is hydrolyzed to dADP and inorganic phosphate (Pi), products that are sequentially released and associated with changes in myosin structure. The dADP is re-phosphorylated to dATP, primarily by creatine kinase such that the triphosphate form is repeatedly replenished. The release of (d)ADP from myosin is considered a rate limiting process of the crossbridge cycle during contraction, especially under load (tension). Since contraction is stronger and faster with dATP (vs. ATP), the M.(d)ADP state is an important part of the crossbridge cycle to study as this therapeutic molecule is developed. Also, using dATP to perturb myosin dynamics presents a unique opportunity to study the thermodynamics and kinetics of cross-bridge cycling. Our biophysical studies have shown that dATP influences multiple chemomechanical states of myosin. We recently reported that myosin is active to a greater extent in both relaxed and contracting muscle in the presence of elevated

dATP [29]. dATP also increases the NTPase rate in muscle [30], results in faster shortening contraction, and increases the motility of f-actin on myosin-coated surfaces [31]. We have reported on the kinetics of nucleotide binding and actin-myosin dissociation comparing ATP and dATP [25]. We did not observe differences in either of those kinetic parameters. However, the rates of force development, NTPase, and motility of f-actin (on myosin-coated surfaces) are all significantly enhanced by dATP. The rate limiting process in all of these measurements is likely the release of ADP prior to crossbridge detachment. Thus, we have chosen for this study to look at the structural dynamics of the M.(d)ADP state. Through complementary computational and experimental efforts we are systematically surveying the effects of dATP/dADP throughout the chemomechanical cycle. In a prior molecular dynamics study of pre-powerstroke *D. discoideum* myosin II, we found that substitution of dADP for ADP altered the conformational distribution of myosin heads to favor actin binding (this study corresponded to post-hydrolysis step 2 in Figure 1C) [31]. Here, we compare the dynamics of myosin in the post-powerstroke state in the presence of ADP versus dADP (step 4 in Figure 1C). These simulations provided information on the structural changes that may precipitate the release of ADP, an important step in the cross-bridge cycle. Comparisons of simulations with dADP in the active site are used as a tool to probe how changes in the nucleotide binding pocked induce changes in the actin binding surface.

Methods

Model Building Myosin II from *Dictyostelium discoideum* in complex with Mg^{2+} and (d)ADP was simulated in the post-powerstroke state of the myosin chemomechanical cycle. The initial coordinates were obtained from the 2.1 Å X-ray structure for myosin from *D. discoideum* in complex with Mg^{2+} and ADP (PDB ID: 1MMA [21]). This structure of myosin was chosen for

comparison with our earlier simulations examining the dynamics of *D. discoideum* myosin II in the pre-powerstroke state. That study used initial coordinates obtained from PDB entry 1VOM [20]. Note that the 1MMA and 1VOM structures are both from *D. discoideum* but have 99% sequence identity (the amino acid sequence differs at positions 42, 65, 321, 322, 443, 446, and 737). Residues in the lever arm are missing from both the 1MMA and 1VOM structures, which may bias the starting conformations used in our simulations. However, the converter domain adopts different orientations in the 1VOM and 1MMA structures, and these different orientations correspond to the swinging of the lever arm. This indicates that myosin structures can adequately capture conformational changes during the cross-bridge cycle in the absence of lever arm residues. Crystallographic solvent molecules were removed from the *D. discoideum* structure and missing coordinates were built using *Modeller* [32–34]. The starting structures for simulations containing dADP were built via replacement of the ADP molecule with a dADP molecule. ADP and dADP were parameterized as described previously [31].

Molecular Dynamics Simulations All-atom conventional molecular dynamics (MD) simulations were performed using the *in lucem* molecular mechanics (*il*mm) simulation package with the Levitt *et al*. forcefield [35–37] and associated methods [38]. The modeled structures of post-powerstroke myosin were prepared for simulation in three phases: minimization, solvation, and equilibration. During minimization, hydrogen atoms were modeled onto the crystallographically determined structures and minimized over 500 steps of steepest descent minimization; then all atoms were minimized over 1000 steps of steepest descent minimization. During solvation, the systems were placed in a periodic box that extended 10 Å beyond any protein atom and were solvated with flexible three-center water molecules [39]. The myosin +

(d)ADP systems included ~85,600 atoms placed in 76 Å × 120 Å × 97 Å boxes. The solvent density was set to the experimentally determined density at 310 K (0.99336 g mL^{-1}) [40]. During equilibration, solvent molecules were minimized for 500 steps of steepest descent minimization, equilibrated for 500 steps (1 ps) using the microcanonical (NVE, constant **n**umber of particles, **v**olume, and **e**nergy) ensemble, and minimized for 500 steps of steepest descent minimization. Finally, all protein and ligand atoms were equilibrated for 500 steps (1 ps) using the NVE ensemble. After preparation, 50 nanosecond (ns) long molecular dynamics simulations of the myosin + Mg^{2+} + ADP and myosin + Mg^{2+} + dADP systems were performed in triplicate (6 total simulations, 300 ns net sampling time, Table 1) at 310 K using the NVE ensemble using a 2 fs timestep and a 10 Å force-shifted nonbonded cutoff [41], and structures were saved every picosecond for analysis. The replicates for each system all had the same starting coordinates, but different initial velocities were assigned using a random number seed.

A separate set of control simulations was performed for ADP and dADP in isolation (2 total simulations, 600 ns net sampling time, Table 1). The minimization, solvation, and equilibration protocols for the isolated nucleotide simulations were identical to those used for the myosin + nucleotide simulations described above. Single replicate (n = 1) production simulations for both systems were performed for 300 ns at 310 K using the NVE ensemble, a 2 fs timestep, and a 10 Å force-shifted nonbonded cutoff. Structures were saved every picosecond for analysis. The simulations presented in this study are summarized in Table 1.

Molecular Dynamics Analysis MD simulations were analyzed using the *il*mm software package and custom python scripts. Protein images were rendered with *UCSF Chimera* [42]. 2D dihedral angle maps were discretized into 5° × 5° bins. Conformational entropy of 2D dihedral angle

maps was calculated using Equation 1, where R is the gas constant and p_i is the fraction of the ensemble that sampled each 5° × 5° bin.

$$S = -R \sum_i p_i ln(p_i)$$

Equation 1

The percent coverage of 2D dihedral angle maps corresponds to the percent of 5° × 5° bins sampled at least once during the simulations. The solvent accessible surface area was calculated using the method of Lee and Richards [43]. Contacts were identified by calculating interatomic distances; atoms were considered in contact with one another if their interatomic distance was < 5.4 Å (two carbon atoms) or < 4.6 Å (two non-carbon atoms) and hydrogen bonds were identified if the donor– acceptor distance was < 2.6 Å and the angle formed by the donor, hydrogen, and acceptor was within 45.0° of linearity. The first 10 ns of the myosin + nucleotide simulations were excluded from all analyses to allow for equilibration. The first ns of the isolated nucleotide simulations were excluded from all analyses.

Table 1. Inventory of simulations presented in this study

System	Replicates (*n*)	Length (nanoseconds)
Myosin (1MMA) + Mg^{2+} + ADP	3	50
Myosin (1MMA) + Mg^{2+} + dADP	3	50
Isolated ADP	1	300
Isolated dADP	1	300

Results

ADP and dADP were dynamically distinct. The difference between the structure of ADP and dADP occurs at the 2’ position of the ribose ring (Figure 2A). In ADP a hydroxyl group is

attached to C2', while in dADP, this hydroxyl group is replaced by a hydrogen atom. Although ADP and dADP only differ by a single hydroxyl group on the ribose ring, the two nucleotides sampled different conformations within the nucleotide binding pockets. We defined 6 dihedral angles of the nucleotides: θ_1 (O1B-PB-O3A-PA), θ_2 (PB-O3A-PA-O5'), θ_3 (O3A-PA-O5'-C5'), θ_4 (PA-O5'-C5'-C4'), θ_5 (O5'-C5'-C4'-O4'), θ_6 (O4'-C1'-N9-C8) and organized them into three dihedral angle maps that reveal accessible conformations of the nucleotides: θ_1 vs. θ_2, θ_3 vs. θ_4, and θ_5 vs. θ_6 (Figure 2B). We quantified the conformational sampling of the nucleotides by calculating the conformational entropy (Table 2) and percent coverage (Table 3) of each of these maps, analogous to what has been done with proteins [44]. dADP was more flexible than ADP, sampling a greater number of conformations and adopting a single stable conformation by the end of the simulations. To determine whether the observed differences in sampling were due to intrinsic differences in the dynamics of the nucleotides, we performed additional simulations of either ADP or dADP alone in a water box. We did not observe differences in the conformational distributions of ADP and dADP in these control simulations (Figure S1), thus the differences observed in the myosin:nucleotide simulations can be attributed to unique interactions between the nucleotides and myosin (Figure S1, Table 2, Table 3). In the absence of the hydroxyl group, dADP had altered electrostatic interactions with myosin. The altered electrostatics within the binding pocket caused ADP and dADP to form distinct sets of interactions with myosin. Contacts formed between the phosphate groups of the nucleotides and the p-loop of myosin (residues 179-186) were the most stable (Figure 3A, Table S1), but ADP formed more frequent interactions with

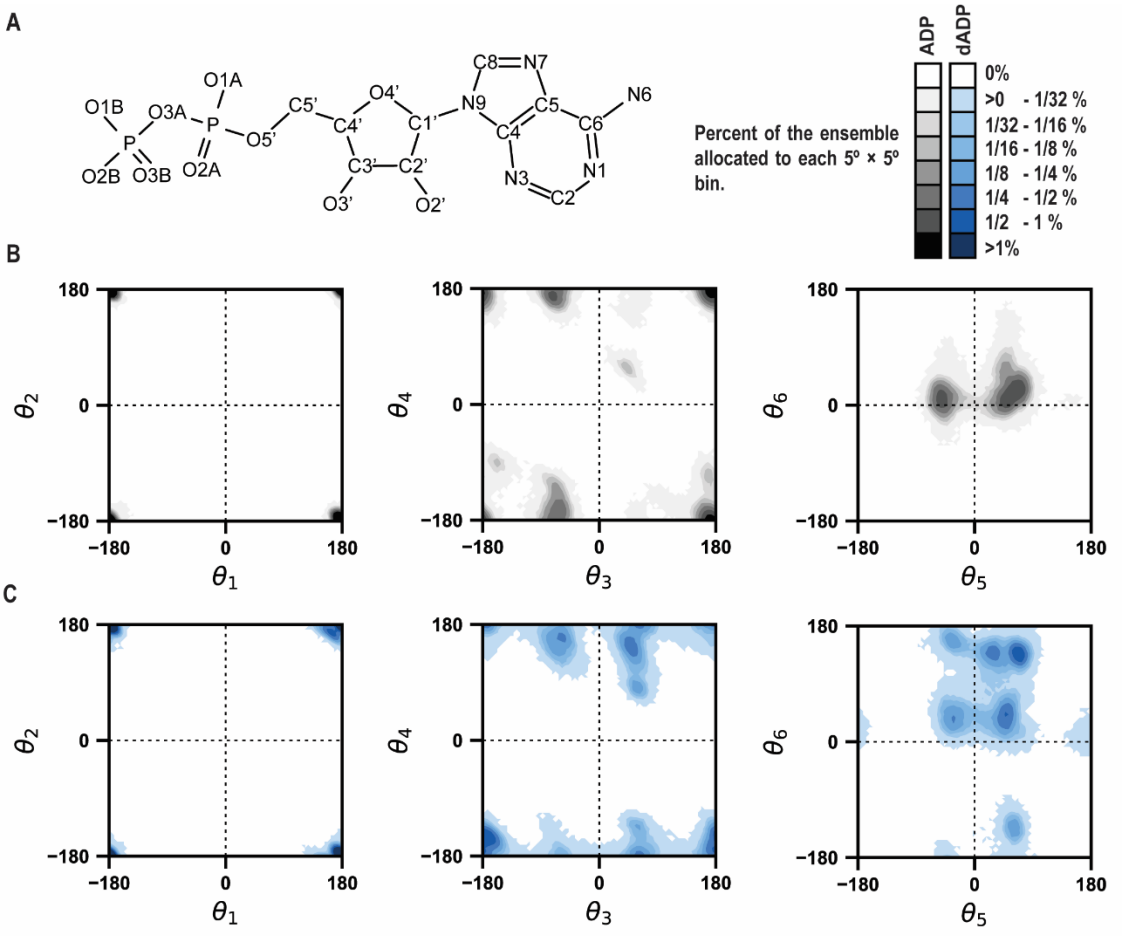

Figure 2: Conformational sampling of ADP and dADP. Six dihedral angles were defined for both nucleotides: θ_1 (O1B-PB-O3A-PA), θ_2 (PB-O3A-PA-O5'), θ_3 (O3A-PA-O5'-C5'), θ_4 (PA-O5'-C5'-C4'), θ_5 (O5'-C5'-C4'-O4'), θ_6 (O4'-C1'-N9-C8) (A). These angles were organized into three maps for ADP (B) and dADP (C). Each map is a two- dimensional histogram (5°×5° bins) of the conformations sampled by the nucleotides in the nucleotide + myosin simulations (data from the three replicate simulations are combined). The color of each bin indicates the percent of the ensemble that sampled the bin.

Table 2. Conformational entropy of ADP and dADP

Dihedral Pair	ADP cal mol^{-1} K^{-1}	dADP cal mol^{-1} K^{-1}	ADP + myosin cal mol^{-1} K^{-1}	dADP + myosin cal mol^{-1} K^{-1}
θ_1 vs. θ_2	13.1	13.0	6.37	7.15
θ_3 vs. θ_4	12.2	12.3	11.5	12.7
θ_5 vs. θ_6	12.3	12.2	11.6	13.0

Table 3. Percentage of dihedral maps sampled by ADP and dADP

Dihedral Pair	ADP %	dADP %	ADP + myosin %	dADP + myosin %
θ_1 vs. θ_2	62	60	3	4
θ_3 vs. θ_4	40	40	29	31
θ_5 vs. θ_6	46	42	22	34

N-terminal p-loop residues (180, 181) while dADP formed more frequent interactions with C-terminal p-loop residues (183, 184). dADP formed interactions with switch 1 residues (233-240) more frequently than ADP (Figure 3A). ADP formed transient interactions with the loop that connects the transducer to the SH1 and SH2 helices (residues 657-668) more frequently than dADP. Neither nucleotide interacted with switch 2 residues (residues 454-459) for a significant fraction of the simulation time. The combined effects of these altered interactions caused ADP to sample conformations similar to the crystallographic structure (Figure 3B and 3C), but both the sugar and purine rings of dADP were flexible and formed transient, heterogeneous interactions with myosin residues (Figure 3B and 3D). Our results suggest that the loss of a hydroxyl group in dADP alters electrostatic interactions within the binding pocket, causing ADP and dADP to have distinct preferences for myosin residues to interact with. Though we did not observe statistically significant differences in contact frequencies, ADP and dADP preferentially interacted with myosin residues on opposing sides of the nucleotide binding pocket (Figure 3).

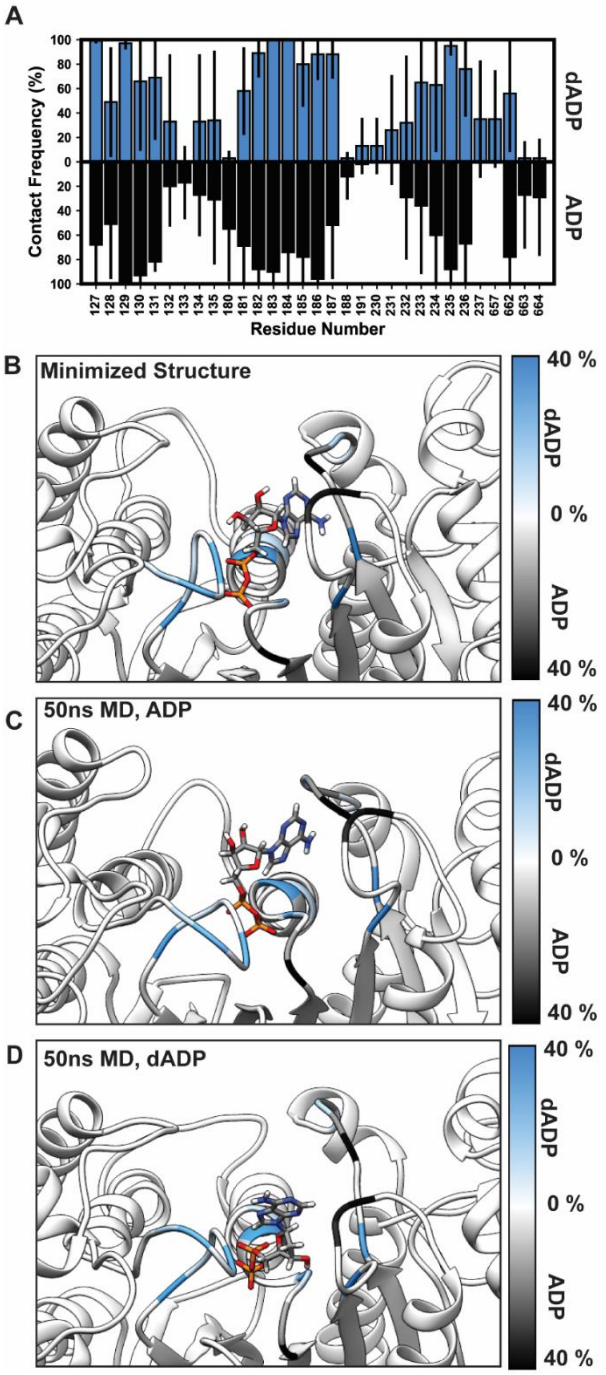

Nucleotide-dependent sampling in the post-powerstroke state. Myosin and the chemomechanical cycle itself are subject to significant allosteric regulation: changes in interactions at the actomyosin interface as well as changes among the contents of the nucleotide binding pocket are transmitted through the protein complex and precipitate the large-scale conformational changes associated with the power and recovery strokes. This allosteric control was observed in our ADP and dADP simulations: the changes in contacts made by dADP relative to ADP were associated with distinct dynamics in myosin. These distinct dynamics were not restricted to the vicinity of the nucleotide binding pocket: conformational changes were observed throughout the protein.

Figure 3. Nucleotide-Myosin interactions. (A) Each bar corresponds to an interaction between ADP (black bars) or dADP (blue bars) and residues in myosin (x-axis). The height of each bar is proportional to the percentage of the simulation time (averaged across the three replicate simulations) that the contact was observed, error lines denote standard deviation. In panels B-D, residues in myosin are colored according to the difference in contact frequency between ADP and dADP. Residues that interacted more

frequently with ADP are colored black and residues that interacted more frequently with dADP are colored blue. The average differences in contact frequency were mapped onto the minimized starting structure (B) and the endpoints of one myosin+ADP simulation (C) and one myosin+dADP simulation (D).

To identify differences in the structure in the presence of different nucleotides, we calculated the C_α root-mean-squared deviation (RMSD) of all C_α atoms after alignment to all C_α atoms (Figure 4A-F). Over the course of the 50 ns simulations, the myosin heads that bound ADP sampled conformations within 8 Å of the minimized starting structure while the myosins that bound dADP sampled conformations within 6 Å of the minimized starting structure (Figure 4A,B). Residues within the unstructured N-terminal domain, SH3

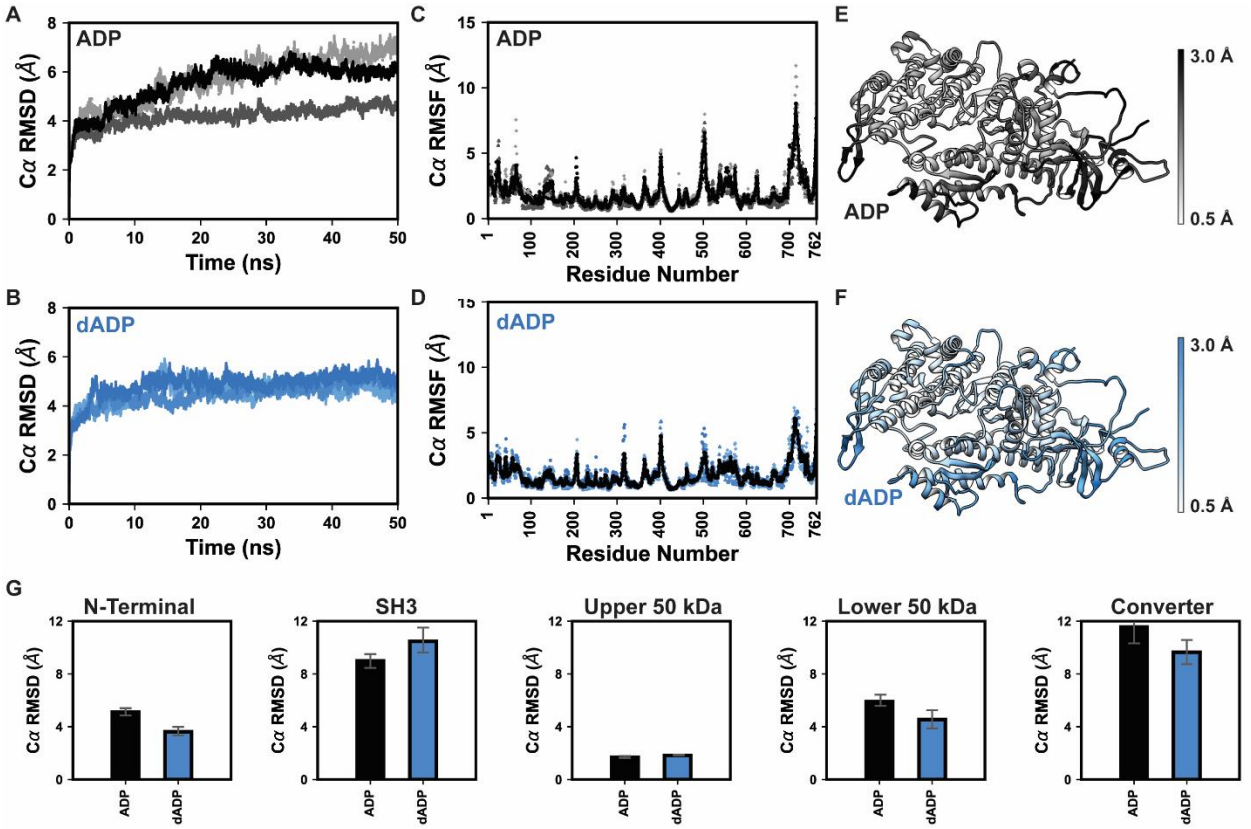

Figure 4: Conformational sampling in MD simulations of post-powerstroke myosin. The C_α RMSD of the myosin heads relative to the minimized starting structure was calculated as a function of time (A: ADP; B: dADP) and residue number (C,E: ADP; D,F: dADP). In A-D, results from replicate simulations are shown in shades of grey (ADP) or blue (dADP). In C-D, the average results from the replicate simulations are plotted as a continuous, thick back line. The average C_α RMSF values per residue are mapped onto the minimized crystal structure in panels E and F. (G) After alignment of the trajectories to the most stable residues, we also calculated the average RMSD (averaged both across the duration of the simulation and across replicate simulations) for specific subdomains in myosin. The five regions were the N-terminal domain (10-15, 99-112, 137-142, and 155-168), SH3 domain (residues 34-37, 48-55, 59-63, 70-73, and 77-80), upper 50 kDa domain (residues 210-226, 265-268, 278-287, 290-295, 301-303, 320-334, 338-356, 373-382, 386-394, 411-440, 594-601, 606-613, 615-618) the lower 50 kDa domain (residues 466-494, 506-534, 540-551, 567-580, 584-589, and 630-647), and the converter domain (residues 722-730 and 748:753) Those average values are reported for the ADP (black bars) and dADP (blue bars) simulations.

domain, and the converter domain (which does not adopt a completely folded structure in 1MMA, likely due to truncated lever arm residues) contributed the most to the deviation from the crystal structure (Figure 4C-F) although conformational differences within the motor were also observed. To identify conformational changes within the subdomains of the myosin head, we performed a second RMSD calculation, where the residues that were the least mobile were used to align the trajectories. The residues chosen were those with C_α RMSFs < 1.2 Å in both the ADP and dADP simulations (Figure 4C-F) and are summarized in Table S2. After alignment, we calculated the C_α RMSDs of 5 regions of myosin. We only calculated the RMSDs for residues that formed stable secondary structure motifs in the crystal structure. The five regions were the N-terminal domain, SH3 domain, upper 50 kDa domain, the lower 50 kDa domain, and the converter domain (Figure 4G). Using these alignments, we calculated the average RMSD across the replicate simulations. The upper 50 kDa had similar flexibility in the ADP and dADP simulations. The N-terminal, lower 50 kDa, and converter domains experienced greater deviations from the minimized crystal structure in the ADP simulations than the dADP simulations. The SH3 domain experienced greater deviation from the minimized structure in the

dADP simulations than in the ADP simulations. This suggests that changing the nucleotide bound to myosin can affect the dynamics of the entire head domain. Although nucleotide-induced differences in the N-terminal and converter domains may exist, these regions are mostly unstructured in these simulations (and the crystal structure) due to the absence of the lever arm residues. Similarly, the SH3 domain is flexible and known to participate in energy transduction in myosin, but its specific roles have not been definitively established [45].

We observed distinct myosin conformations when ADP or dADP were in the binding pocket, although the difference in RMSD of these regions were not statistically significant. The replicate simulations have not converged to a self-consistent [46] ensemble: the 50 ns endpoint conformations may represent local minima in conformational space. It is possible that there exists a conformation of myosin that is a global minimum in the presence of either ADP or dADP. However, our simulations indicate that the myosin+ADP and myosin+dADP have distinct conformational landscapes. Both sets of simulations began from the same crystallographic structure, yet the myosin+ADP and myosin+dADP simulations adopted distinct conformations, and these distinct conformations were populated among the triplicate runs.

dADP stabilized the relative orientation of the upper and lower 50 kDa domains.

To better understand how myosin interactions with actin may be altered, we focused our analysis on the conformational effects that dADP had on the actin binding cleft, formed at the interface of the upper and lower 50 kDa domains. Of those two subdomains in myosin, the lower 50 kDa domain experienced the greatest change relative to the crystal structure (Figure 4G). This corresponded to a twisting motion that affected the relative orientation of the upper and lower 50 kDa domains (Figure 5). In the myosin + ADP simulations, the helix-loop-helix (HLH) of the

lower 50 kDa domain and loop 3 twisted in the direction of loop 2; the β-hairpin lost contacts with the relay helix and projected towards the solvent; and switch 2 became more extended (Figure 5). These residues were also mobile in the myosin + dADP simulations, but the extent of motion was reduced relative to the myosin + ADP simulations. These data suggest that the actin binding cleft of myosin adopts distinct conformational ensembles in the presence of ADP versus dADP.

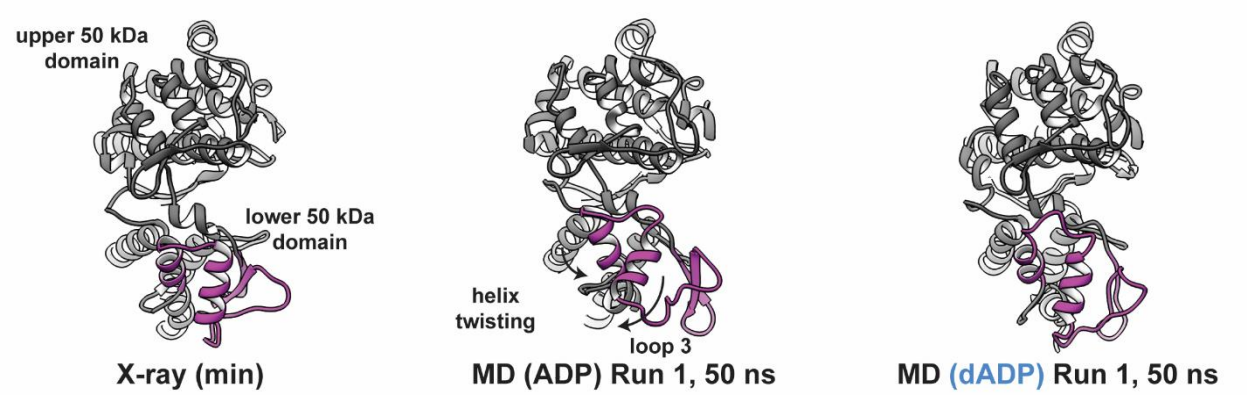

Figure 5: dADP-induced conformational changes in the actin binding cleft. The panels include ribbon structures of the myosin head for the minimized X-ray structure (left) and representative snapshots from MD simulations with ADP (center) or dADP (right). For clarity, the structures of myosin have been clipped such that the portion of the structure between the nucleotide binding pocket and converter domain is not visible here. The myosin heads are oriented with the actin binding cleft facing forward and the nucleotide binding pocket on the right. The nucleotides are represented as spheres. Residues in the lower 50 kDa domain that were associated with the relative twisting motion of the upper and lower 50 kDa domains are colored magenta.

dADP altered the actin binding site and increased the exposure of charged residues. The conformational changes to the actin binding cleft caused by the relative twisting of the upper and lower 50 kDa domains altered the properties of the actin binding cleft. We tracked the solvent accessible surface area of the actin binding residues within the cleft. Actin binding residues were chosen based on their modeled contacts in cryoEM structures of the

actomyosin complex. dADP induced a shift in the solvent accessible surface area of the actin binding cleft. In all simulations performed, the actin binding cleft was flexible and experienced a breathing motion causing fluctuations in the solvent accessible surface area of the actin binding cleft over time (Figure 6A-B). The two nucleotides induced shifts in the solvent exposure of actin binding residues. In the simulations with dADP, there was an increase in the solvent exposure of polar atoms within charged actin binding residues (Figure 6A). The charged residues in loop 2, including R620 and K623, contributed the most to this increase (Figure 6C). In the simulations with ADP, there was an increase in the solvent exposure of nonpolar atoms of actin binding residues (Figure 6B). Neither the 1MMA structure nor these simulations contain actin, which should be bound to myosin in this state of the chemomechanical cycle. Thus, the observed differences in structural properties of the actin binding cleft may be different when myosin is bound to actin.

dADP also induced changes in the geometry of the actin binding cleft. To probe the cleft geometry in our simulations, we calculated interatomic distances between residues within the cleft. Klein *et al.* engineered Cys residues (at residue positions 270, 366, 401, 416, 463, 537, 583, and 587) into *D. discoideum* S1 to probe the geometry of the actin binding cleft [47]. They labeled these Cys residues with IPSL [3-(2-Iodoacetamido)-2,2,5,5-tetramethyl-1-pyrolidinyloxy] or MSL [N-(1-Oxyl-2,2,6,6-tetramethyl-4-piperidinyl)maleimide] to probe 2 'inner-cleft' distances (270-463 and 416-583) and 3 'outer-cleft' distances (366-537, 401-537, and 416-537) with site-directed spin labeling. We calculated distances among the same residues probed by Klein *et al*. for those same residue pairs. This calculation is not a direct comparison with the results of Klein *et al.* as we did not model either Cys residue or spin labels into our simulations. The interatomic distances were instead calculated between the C_α atoms of the

residues at those positions in the sequence (Figure 6D). As was observed for the solvent accessible surface area calculations, the interatomic distances fluctuated over time, and those fluctuations were associated both with the breathing motion of the cleft and the relative twisting of the upper and lower 50 kDa domains. For both the ADP and dADP simulations, the 'outer' portion of the cleft was more flexible than the 'inner' portion. All three 'outer' cleft distance distributions were shifted towards shorter distances (corresponding to a more closed cleft) in the dADP simulations. The average shift was ~2Å for all three distances. Both of the 'inner' cleft distance distributions were shifted toward larger values (corresponding to a more open cleft) in the dADP simulations. The average shift was ~1Å for both distances (Figure 6D).

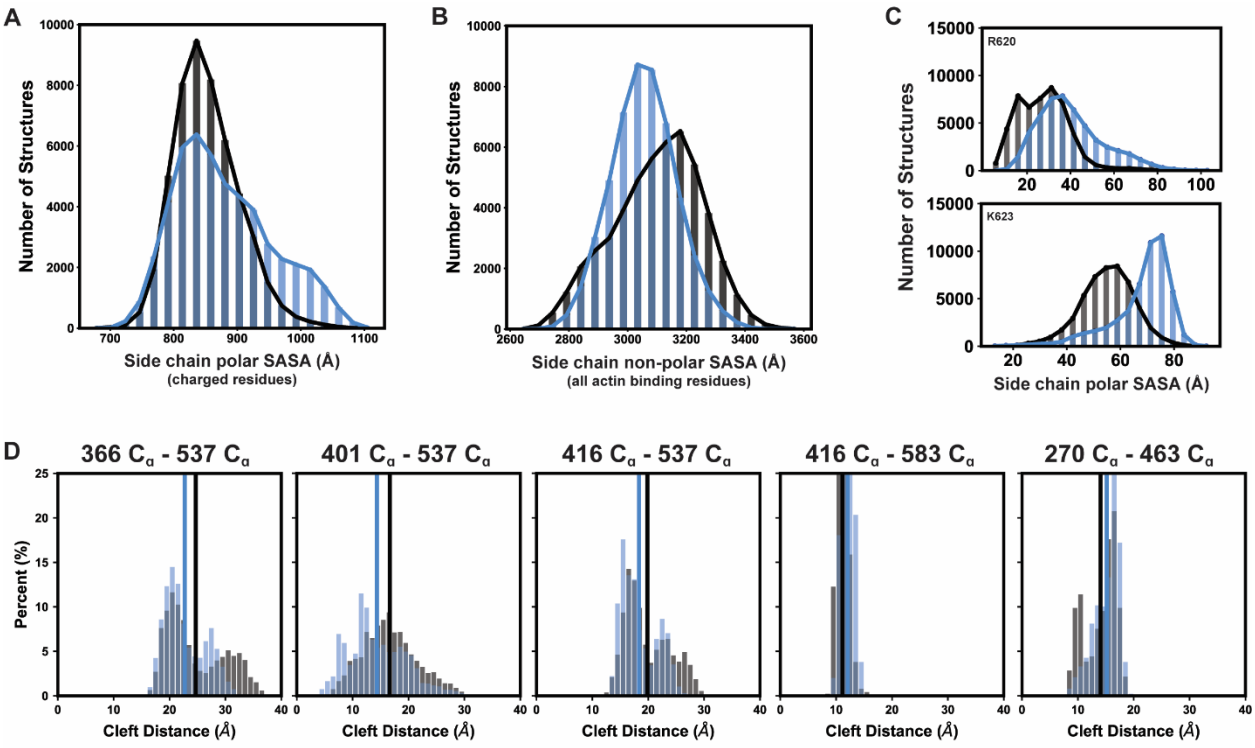

Figure 6: The structural features of the actin binding cleft were nucleotide-dependent. Histograms of the solvent accessible surface area of polar atoms within charged residues at the actin binding surface (A), nonpolar atoms within actin binding residues (B) and of specific residues within loop 2 (C) show that the actin binding surface of myosin changes when myosin is bound ADP (black bars) versus dADP (blue bars). Similarly, the geometry of the actin binding cleft (D), as monitored by interatomic distances

at 6 residues, was nucleotide dependent. The colors in D are the same as the other panels and the thick vertical bars correspond to the average ADP and dADP distances.

The conformational effects of ADP and dADP propagate through the S1 head. In the simulations described here, we observed conformational differences in the dynamics of myosin + ADP versus myosin + dADP (Figure 2). Distinct nucleotide dynamics were associated with changes in the conformation (Figure 5) and structural properties (Figure 6) of the actin binding cleft. We analyzed the contacts formed between amino acid side chains to track how conformational changes in the nucleotide binding pocket propagated through the structure. We generated side chain – side chain contact maps for each trajectory (Figure 7A). The strength of each contact corresponds to the fraction of the simulation that the contact was observed. For each contact, we used a two-tailed Student's t-test to evaluate whether the there was a statistically significant difference in the strength of the contact in the ADP or dADP simulations. Finally, we mapped contacts with significantly ($p \leq 0.05$) different strengths onto the 1MMA crystal structure to observe how they propagated through the structure (Figure 7B, Table S3). The nucleotide-specific contacts clustered within three regions of the structure: the nucleotide binding pocket (see also Figure 3A), the HLH motif of the lower 50 kDa domain (see also Figure 5), and the L and O helices of the upper 50 kDa domain (Figure 7B). The cluster of nucleotide-specific contacts within the binding pocket reflected the distinct conformational ensembles populated by ADP and dADP. The cluster of nucleotide-specific contacts within the lower 50 kDa domain correspond to the twisting motion observed more frequently in the ADP simulations. The cluster of nucleotide-specific contacts within the upper 50 kDa domain correspond to changes in the packing around the L and O helices. Specifically, residues 279-308 and 594-618 form clusters of short α-helices that pack against opposite sides of the central L and O helices. dADP induced subtle shifts in side chain packing among these sets of residues.

Several residues within the vicinity of the nucleotide binding pocket connected the three clusters of nucleotide-specific contacts and include residues 180-3, 186, 194, 214, 218-9, 230-3, 238-9, and 456. Of these, the contact with the biggest difference in the ADP and dADP simulations was formed between R238 and S456. These residues are in switch 1 and switch 2, respectively, and they connect the nucleotide-binding pocket and lower 50 kDa domain. In the dADP simulations, a hydrogen bond formed between the side chains of these residues and that hydrogen bond was not observed in the ADP simulations. R238 also formed a salt bridge with E459 in both the ADP and dADP simulation but occurred much more frequently in the dADP simulations (Figure 7B). Formation of a hydrogen bond between the two residues reduced the conformational flexibility of switch 2: in the dADP simulations loop 2 formed a more compact, though disordered, structure, which may in turn reduce the conformational flexibility of the lower 50 kDa domain. The dADP-induced conformational changes within the binding pocket allowed for the formation of the 238-456 contact and associated stabilization of the lower 50 kDa domain structure.

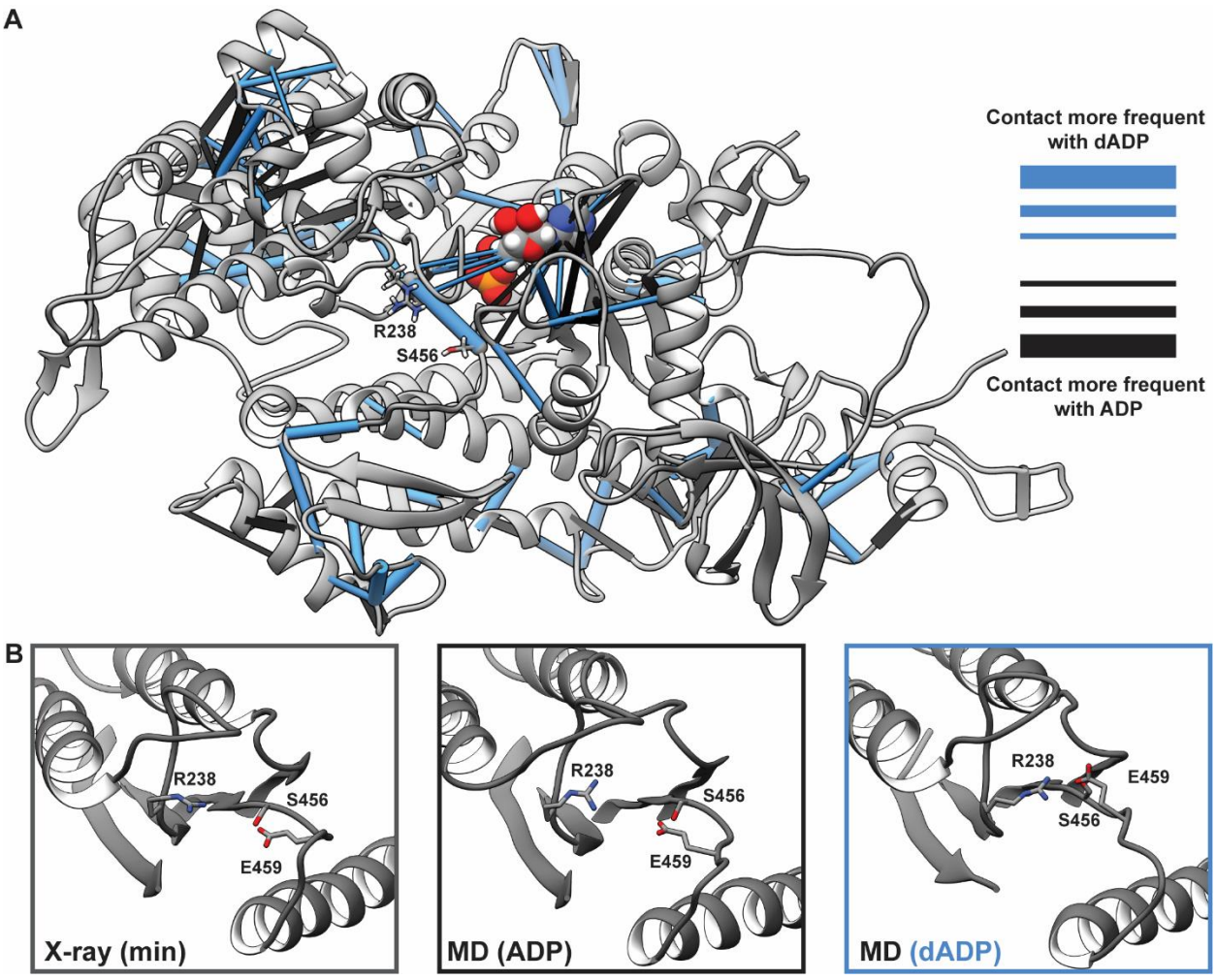

Figure 7: dADP influences the residue-residue interaction network in myosin. (A) Inter-residue contacts in myosin that had significantly different frequencies in the ADP and dADP simulations are mapped onto the minimized crystal structure. Those contacts are represented as pipes and are colored black when observed more frequently in the ADP simulations or blue when observed more frequently in the dADP simulations. The pipe diameter is proportional to the difference of the contacts' frequency in the ADP or dADP simulations. All contact differences involving ADP or dADP are also mapped, independent of statistical significance. (B) Snapshots the minimized X-ray structure (left), and the endpoints of an ADP (middle) and dADP (right) simulation highlight the influence of the bound nucleotide on contacts made by R238, S456, and E459.

Discussion

During the powerstroke, myosin forms distinct sets of interactions with actin. These interactions precipitate release of catalytic byproducts (P_i, Mg, and ADP) from the nucleotide binding pocket, which, in turn, results in changes in myosin structure. The crystal structure that

serves as the basis for these simulations, 1MMA, models the post-powerstroke state after release of Pi, which corresponds to a state of myosin strongly bound to actin and ADP less tightly associated with myosin [7]. The simulations described here model events that occur prior to release of Mg^{2+}. Since neither the 1MMA crystal structure nor our simulations contain actin, our current model of post-powerstroke dynamics does not capture the allosteric effects of the actomyosin interaction on myosin dynamics. Instead, we have focused on structural changes imposed on the myosin motor domain by dADP binding in place of ADP. The therapeutic potential of dATP is promising: the simulations described here predict some molecular mechanisms by which dATP and its catalyzed form exert their effects. However, three factors limit the results of these simulations. First, our triplicate simulations were performed for 50 ns each: longer sampling times may indicate more significant structural effects of dADP. Second, our simulations of the ADP state of myosin were performed in the absence of actin; in fact, the x-ray model used as a bases for these simulations was similarly devoid of actin. Third, this study focuses on the ADP state of myosin. The sets of simulations we have performed to date have quantified locals sampling within specific chemomechanical states over short time scales. It remains possible that the most significant effects of dATP on the chemomechanical cycle occur in a state yet to be simulated, in a transition between conformational states (such as phosphate release or the swing of the lever arm), or only in the presence of other thick/thin filament proteins.

Our simulations predict two ways in which dADP perturbs the dynamics of the chemomechanical cycle. First, the current results support our proposed mechanism that dADP exerts its effects on muscle contraction by altering the nature of the actomyosin interaction [29,31]. In simulations with dADP, there was an increase in the solvent exposure of polar atoms

in the charged residues of the actin binding cleft, and the cleft adopted a more closed conformation (Figure 6). This suggests that dADP stabilizes conformations of the cleft that promote the formation of strong interactions with actin and that the conformational ensemble observed in our simulations is one optimized for actin binding. These results bear similarities to those from simulations of pre-powerstroke myosin [31] and of the ATP state of myosin [28]. All three sets of simulations show that dATP (or dADP) alter the actin binding surface of myosin and promote the exposure of positively charged residues. The structure of the actin binding cleft was more flexible in simulations with ADP, and the prominent change to the structure was a twisting motion between upper and lower 50 kDa domains. This twisting motion, which was dampened in the dADP simulations, would likely be impeded in the actomyosin complex, but may play a role in the early stages of the relaxation of myosin heads as they detach from the thick filament. Our simulations also indicate that there are differences in the affinity of myosin for ADP versus dADP. dADP was more conformationally heterogeneous than ADP (Figure 2). This increase in conformational entropy may facilitate release of dADP from the binding pocket at a faster rate than ADP, expediting relaxation. We propose that these dual mechanisms, increased myosin interaction with actin and faster dADP release, allow dATP to optimize cross-bridge cycling when it is the energetic substrate for contraction.

Our analysis also identified several residues that lie along allosteric pathways that communicate structural information between the functional sites of the myosin motor, namely the actin binding cleft, the nucleotide binding pocket, and the converter domain, for example the interaction observed between R238 and S456 in the dADP simulations. The heightened flexibility of dADP reorganized both nucleotide:protein and protein:protein interactions within the binding pocket and allowed for residues in switch 1 (R238) and switch 2 (S456, E459) to

interact with one another. Formation of these interactions was associated with a more compact conformation of the loop containing switch 2 and a dampening of the twisting motion of the upper and lower 50 kDa domains. R238 corresponds to R243 in human MYH7, S456 corresponds to A463, and E459 corresponds to E466. R238 is a highly conserved residue in switch 1, and mutation of this position has been associated with Usher syndrome [48]. Morales and coworkers introduced several mutations to probe the R238-E459 salt bridge of chicken myosin. They found that salt bridge formation was required for ATP hydrolysis and that elimination of the salt bridge was associated with 'defective' interactions between myosin and actin [49–51]. Sutoh and coworkers also studied a R238A mutation in *D. discoideum* myosin II; they found that R238A reduced both ATPase activity and myosin motility [52]. Our molecular-level observations further suggest that dATP enhances formation of electrostatic interactions between switch 1 and 2 and that at least part of its mechanistic action is to alter allosteric communication in myosin through this pathway.

Acknowledgements

We thank Dr. Sarah Nowakowski for preparing and running some initial simulations. This work was supported by NIH R01 HL128368, NIH R56 AG055594, NIH RM1 GM131981 and NIH U01 HL122199 to MR, EU 777204 to MR and MAG, and NIH R0150789 to VD.

References

[1] H.L. Sweeney, D.W. Hammers, Muscle Contraction, Csh Perspect Biol. 10 (2018) a023200. https://doi.org/10.1101/cshperspect.a023200.

[2] M. Vicente-Manzanares, X. Ma, R.S. Adelstein, A.R. Horwitz, Non-muscle myosin II takes centre stage in cell adhesion and migration., Nat Rev Mol Cell Biology. 10 (2009) 778–90. https://doi.org/10.1038/nrm2786.

[3] M.A. Titus, Myosin-Driven Intracellular Transport., Csh Perspect Biol. 10 (2018) a021972. https://doi.org/10.1101/cshperspect.a021972.

[4] M.J.T. Cope, J. Whisstock, I. Rayment, J. Kendrick-Jones, Conservation within the myosin motor domain: implications for structure and function, Structure. 4 (1996) 969–987. https://doi.org/10.1016/s0969-2126(96)00103-7.

[5] A. Cammarato, C.M. Dambacher, A.F. Knowles, W.A. Kronert, R. Bodmer, K. Ocorr, S.I. Bernstein, Myosin Transducer Mutations Differentially Affect Motor Function, Myofibril Structure, and the Performance of Skeletal and Cardiac Muscles, Mol Biol Cell. 19 (2008) 553–562. https://doi.org/10.1091/mbc.e07-09-0890.

[6] A. Houdusse, V.N. Kalabokis, D. Himmel, A.G. Szent-Györgyi, C. Cohen, Atomic Structure of Scallop Myosin Subfragment S1 Complexed with MgADP, Cell. 97 (1999) 459–470. https://doi.org/10.1016/s0092-8674(00)80756-4.

[7] H.L. Sweeney, A. Houdusse, Structural and Functional Insights into the Myosin Motor Mechanism, Annu Rev Biophys. 39 (2010) 539–557. https://doi.org/10.1146/annurev.biophys.050708.133751.

[8] J.M. Muretta, J.A. Rohde, D.O. Johnsrud, S. Cornea, D.D. Thomas, Direct real-time detection of the structural and biochemical events in the myosin power stroke, Proc National Acad Sci. 112 (2015) 14272–14277. https://doi.org/10.1073/pnas.1514859112.

[9] H. Sugi, T. Akimoto, S. Chaen, Basic Properties of ATP-Induced Myosin Head Movement in Hydrated Myosin Filaments, Studied Using the Gas Environmental Chamber, Micron. 112 (2018) 15–25. https://doi.org/10.1016/j.micron.2018.06.003.

[10] T. Kraft, E. Mählmann, T. Mattei, B. Brenner, Initiation of the power stroke in muscle: Insights from the phosphate analog AlF4, P Natl Acad Sci Usa. 102 (2005) 13861–13866. https://doi.org/10.1073/pnas.0504026102.

[11] M.S. Woody, D.A. Winkelmann, M. Capitanio, E.M. Ostap, Y.E. Goldman, Single molecule mechanics resolves the earliest events in force generation by cardiac myosin, Elife. 8 (2019) e49266. https://doi.org/10.7554/elife.49266.

[12] Y. Yang, S. Gourinath, M. Kovács, L. Nyitray, R. Reutzel, D.M. Himmel, E. O'Neall-Hennessey, L. Reshetnikova, A.G. Szent-Györgyi, J.H. Brown, C. Cohen, Rigor-like Structures from Muscle Myosins Reveal Key Mechanical Elements in the Transduction Pathways of This Allosteric Motor, Structure. 15 (2007) 553–564. https://doi.org/10.1016/j.str.2007.03.010.

[13] C. Karatzaferi, N. Adamek, M.A. Geeves, Modulators of actin-myosin dissociation: basis for muscle type functional differences during fatigue, Am J Physiol-Cell Ph. 313 (2017) C644–C654. https://doi.org/10.1152/ajpcell.00023.2017.

[14] S.M. Mijailovich, D. Nedic, M. Svicevic, B. Stojanovic, J. Walklate, Z. Ujfalusi, M.A. Geeves, Modeling the Actin.myosin ATPase Cross-Bridge Cycle for Skeletal and Cardiac Muscle Myosin Isoforms., Biophys J. 112 (2017) 984–996. https://doi.org/10.1016/j.bpj.2017.01.021.

[15] L.M. Bond, D.A. Tumbarello, J. Kendrick-Jones, F. Buss, Small-molecule inhibitors of myosin proteins, Future Medicinal Chemistry. (2013) 41–52. https://doi.org/10.4155/fmc.12.185.

[16] M. Regnier, D.M. Lee, E. Homsher, ATP Analogs and Muscle Contraction: Mechanics and Kinetics of Nucleoside Triphosphate Binding and Hydrolysis, Biophys J. 74 (1998) 3044–3058. https://doi.org/10.1016/s0006-3495(98)78012-9.

[17] M. Regnier, E. Homsher, The Effect of ATP Analogs on Posthydrolytic and Force Development Steps in Skinned Skeletal Muscle Fibers, Biophys J. 74 (1998) 3059–3071. https://doi.org/10.1016/s0006-3495(98)78013-0.

[18] N. Sasaki, R. Ohkura, K. Sutoh, Dictyostelium myosin II as a model to study the actin–myosin interactions during force generation, J Muscle Res Cell M. 23 (2002) 697–702. https://doi.org/10.1023/a:1024415409406.

[19] H.M. Berman, J. Westbrook, Z. Feng, G. Gilliland, T.N. Bhat, H. Weissig, I.N. Shindyalov, P.E. Bourne, The Protein Data Bank, Nucleic Acids Res. 28 (2000) 235–242. https://doi.org/10.1093/nar/28.1.235.

[20] C.A. Smith, I. Rayment, X-ray Structure of the Magnesium(II)·ADP·Vanadate Complex of the Dictyostelium discoideum Myosin Motor Domain to 1.9 Å Resolution † , ‡, Biochemistry-Us. 35 (1996) 5404–5417. https://doi.org/10.1021/bi952633+.

[21] A.M. Gulick, C.B. Bauer, J.B. Thoden, I. Rayment, X-ray Structures of the MgADP, MgATPγS, and MgAMPPNP Complexes of the Dictyostelium discoideum Myosin Motor Domain † , ‡, Biochemistry-Us. 36 (1997) 11619–11628. https://doi.org/10.1021/bi9712596.

[22] C.B. Bauer, H.M. Holden, J.B. Thoden, R. Smith, I. Rayment, X-ray Structures of the Apo and MgATP-bound States of Dictyostelium discoideum Myosin Motor Domain, J Biol Chem. 275 (2000) 38494–38499. https://doi.org/10.1074/jbc.m005585200.

[23] M. Regnier, H. Martin, R.J. Barsotti, A.J. Rivera, D.A. Martyn, E. Clemmens, Cross-Bridge versus Thin Filament Contributions to the Level and Rate of Force Development in Cardiac Muscle, Biophys J. 87 (2004) 1815–1824. https://doi.org/10.1529/biophysj.103.039123.

[24] S.C. Kolwicz, G.L. Odom, S.G. Nowakowski, F. Moussavi-Harami, X. Chen, H. Reinecke, S.D. Hauschka, C.E. Murry, G.G. Mahairas, M. Regnier, AAV6-mediated Cardiac-specific Overexpression of Ribonucleotide Reductase Enhances Myocardial Contractility., Mol Ther J Am Soc Gene Ther. 24 (2015) 240–50. https://doi.org/10.1038/mt.2015.176.

[25] F.S. Korte, J. Dai, K. Buckley, E.R. Feest, N. Adamek, M.A. Geeves, C.E. Murry, M. Regnier, Upregulation of cardiomyocyte ribonucleotide reductase increases intracellular 2 deoxy-ATP, contractility, and relaxation., J Mol Cell Cardiol. 51 (2011) 894–901. https://doi.org/10.1016/j.yjmcc.2011.08.026.

[26] M. Regnier, D.A. Martyn, P.B. Chase, Calcium Regulation of Tension Redevelopment Kinetics with 2-Deoxy-ATP or Low [ATP] in Rabbit Skeletal Muscle, Biophys J. 74 (1998) 2005–2015. https://doi.org/10.1016/s0006-3495(98)77907-x.

[27] S. Kadota, J. Carey, H. Reinecke, J. Leggett, S. Teichman, M.A. Laflamme, C.E. Murry, M. Regnier, G.G. Mahairas, Ribonucleotide reductase-mediated increase in dATP improves cardiac performance via myosin activation in a large animal model of heart failure., Eur J Heart Fail. 17 (2015) 772–81. https://doi.org/10.1002/ejhf.270.

[28] W. Ma, M. Childers, J. Murray, F. Moussavi-Harami, H. Gong, R. Weiss, V. Daggett, T. Irving, M. Regnier, Myosin dynamics during relaxation in mouse soleus muscle and modulation by 2′-deoxy-ATP, J Physiology. 598 (2020) 5165–5182. https://doi.org/10.1113/jp280402.

[29] J.D. Powers, C.-C. Yuan, K.J. McCabe, J.D. Murray, M.C. Childers, G.V. Flint, F. Moussavi-Harami, S. Mohran, R. Castillo, C. Zuzek, W. Ma, V. Daggett, A.D. McCulloch, T.C. Irving, M. Regnier, Cardiac myosin activation with 2-deoxy-ATP via increased electrostatic interactions with actin., P Natl Acad Sci Usa. 116 (2019) 11502–11507. https://doi.org/10.1073/pnas.1905028116.

[30] F. Moussavi-Harami, M.V. Razumova, A.W. Racca, Y. Cheng, A. Stempien-Otero, M. Regnier, 2-Deoxy adenosine triphosphate improves contraction in human end-stage heart failure, J Mol Cell Cardiol. 79 (2015) 256–263. https://doi.org/10.1016/j.yjmcc.2014.12.002.

[31] S.G. Nowakowski, M. Regnier, V. Daggett, Molecular mechanisms underlying deoxy-ADP.Pi activation of pre-powerstroke myosin., Protein Sci Publ Protein Soc. 26 (2017) 749–762. https://doi.org/10.1002/pro.3121.

[32] A. Fiser, A. Šali, Methods in Enzymology, Methods Enzymol. 374 (2003) 461–491. https://doi.org/10.1016/s0076-6879(03)74020-8.

[33] O. Guvench, A.D. MacKerell, Methods in Molecular Biology, Methods Mol Biology Clifton N J. 443 (2008) 63–88. https://doi.org/10.1007/978-1-59745-177-2_4.

[34] A. Šali, T.L. Blundell, Comparative Protein Modelling by Satisfaction of Spatial Restraints, J Mol Biol. 234 (1993) 779–815. https://doi.org/10.1006/jmbi.1993.1626.

[35] D.A.C. Beck, M.E. McCully, D.O.V. Alonso, V. Daggett, in lucem molecular mechanics, University of Washington, Seattle, WA, USA, 2000.

[36] M. Levitt, M. Hirshberg, R. Sharon, V. Daggett, Potential energy function and parameters for simulations of the molecular dynamics of proteins and nucleic acids in solution, Comput Phys Commun. 91 (1995) 215–231. https://doi.org/10.1016/0010-4655(95)00049-l.

[37] M.C. Childers, V. Daggett, Validating Molecular Dynamics Simulations against Experimental Observables in Light of Underlying Conformational Ensembles, J Phys Chem B. 122 (2018) 6673–6689. https://doi.org/10.1021/acs.jpcb.8b02144.

[38] D.A.C. Beck, V. Daggett, Methods for molecular dynamics simulations of protein folding/unfolding in solution, Methods. 34 (2004) 112–120. https://doi.org/10.1016/j.ymeth.2004.03.008.

[39] M. Levitt, M. Hirshberg, R. Sharon, K.E. Laidig, V. Daggett, Calibration and Testing of a Water Model for Simulation of the Molecular Dynamics of Proteins and Nucleic Acids in Solution, J Phys Chem B. 101 (1997) 5051–5061. https://doi.org/10.1021/jp964020s.

[40] G.S. Kell, Precise representation of volume properties of water at one atmosphere, J Chem Eng Data. 12 (1967) 66–69. https://doi.org/10.1021/je60032a018.

[41] D.A.C. Beck, R.S. Armen, V. Daggett, Cutoff Size Need Not Strongly Influence Molecular Dynamics Results for Solvated Polypeptides †, Biochemistry-Us. 44 (2005) 609–616. https://doi.org/10.1021/bi0486381.

[42] E.F. Pettersen, T.D. Goddard, C.C. Huang, G.S. Couch, D.M. Greenblatt, E.C. Meng, T.E. Ferrin, UCSF Chimera?A visualization system for exploratory research and analysis, J Comput Chem. 25 (2004) 1605–1612. https://doi.org/10.1002/jcc.20084.

[43] B. Lee, F.M. Richards, The interpretation of protein structures: Estimation of static accessibility, J Mol Biol. 55 (1971) 379-IN4. https://doi.org/10.1016/0022-2836(71)90324-x.

[44] C.-L. Towse, M. Akke, V. Daggett, The Dynameomics Entropy Dictionary: A Large-Scale Assessment of Conformational Entropy across Protein Fold Space., J Phys Chem B. 121 (2017) 3933–3945. https://doi.org/10.1021/acs.jpcb.7b00577.

[45] B.J. Foth, M.C. Goedecke, D. Soldati, New insights into myosin evolution and classification, Proc National Acad Sci. 103 (2006) 3681–3686. https://doi.org/10.1073/pnas.0506307103.

[46] L. Sawle, K. Ghosh, Convergence of Molecular Dynamics Simulation of Protein Native States: Feasibility vs Self-Consistency Dilemma., J Chem Theory Comput. 12 (2016) 861–9. https://doi.org/10.1021/acs.jctc.5b00999.

[47] J.C. Klein, A.R. Burr, B. Svensson, D.J. Kennedy, J. Allingham, M.A. Titus, I. Rayment, D.D. Thomas, Actin-binding cleft closure in myosin II probed by site-directed spin labeling and pulsed EPR, Proc National Acad Sci. 105 (2008) 12867–12872. https://doi.org/10.1073/pnas.0802286105.

[48] D. Well, S. Blanchard, J. Kaplan, P. Guilford, F. Gibson, J. Walsh, P. Mburu, A. Varela, J. Levilliers, M.D. Weston, P.M. Kelley, W.J. Kimberling, M. Wagenaar, F. Levi-Acobas, D. Larget-Piet, A. Munnich, K.P. Steel, S.D.M. Brown, C. Petit, Defective myosin VIIA gene responsible for Usher syndrome type IB, Nature. 374 (1995) 60–61. https://doi.org/10.1038/374060a0.

[49] H. Onishi, S. -i Kojima, K. Katoh, K. Fujiwara, H.M. Martinez, M.F. Morales, Functional transitions in myosin: Formation of a critical salt-bridge and transmission of effect to the sensitive tryptophan, Proc National Acad Sci. 95 (1998) 6653–6658. https://doi.org/10.1073/pnas.95.12.6653.

[50] Correction, Proc National Acad Sci. 98 (2001) 5369–5369. https://doi.org/10.1073/pnas.111149198.

[51] M. Furch, S. Fujita-Becker, M.A. Geeves, K.C. Holmes, D.J. Manstein, Role of the salt-bridge between switch-1 and switch-2 of Dictyostelium myosin 1 1Edited by A. R. Fersht, J Mol Biol. 290 (1999) 797–809. https://doi.org/10.1006/jmbi.1999.2921.

[52] T. Shimada, N. Sasaki, R. Ohkura, K. Sutoh, Alanine Scanning Mutagenesis of the Switch I Region in the ATPase Site of Dictyostelium discoideum Myosin II †, Biochemistry-Us. 36 (1997) 14037–14043. https://doi.org/10.1021/bi971837i.